A gel phase promotes condensation of liquid P granules in *Caenorhabditis elegans* embryos

Andrea Putnam [1], Madeline Cassani[1], Jarrett Smith[1,2] and Geraldine Seydoux [1]*

RNA granules are subcellular compartments that are proposed to form by liquid–liquid phase separation (LLPS), a thermodynamic process that partitions molecules between dilute liquid phases and condensed liquid phases. The mechanisms that localize liquid phases in cells, however, are not fully understood. P granules are RNA granules that form in the posterior of *Caenorhabditis elegans* embryos. Theoretical studies have suggested that spontaneous LLPS of the RNA-binding protein PGL-3 with RNA drives the assembly of P granules. We find that the PGL-3 phase is intrinsically labile and requires a second phase for stabilization in embryos. The second phase is formed by gel-like assemblies of the disordered protein MEG-3 that associate with liquid PGL-3 droplets in the embryo posterior. Co-assembly of gel phases and liquid phases confers local stability and long-range dynamics, both of which contribute to localized assembly of P granules. Our findings suggest that condensation of RNA granules can be regulated spatially by gel-like polymers that stimulate LLPS locally in the cytoplasm.

L iquid–liquid phase separation (LLPS) is a spontaneous de-mixing process in which molecules partition between condensed and dilute liquid phases[1,2]. LLPS has been proposed to underlie the formation of RNA granules in cells, and several RNA-binding proteins have been found to undergo LLPS in vitro[3]. Some LLPS condensates assembled in vitro mature over time into non-dynamic, gel-like condensates[4–7]. Solidification of liquid phases in RNA granules has been linked to pathological states, as in certain neurodegenerative diseases where RNA granule components become trapped in non-dynamic aggregates[2,8]. Solid cores have also been observed in stress granules, but whether they are byproducts of LLPS or essential structures that support granule assembly is not yet known[9,10]. Here we have investigated a possible role for non-dynamic condensates in the formation of P granules, dynamic RNA granules that form under normal conditions in the germline of *Caenorhabditis elegans*.

P granules were the first cytoplasmic RNA granules reported to display liquid-like behaviors[11]. P granules are roughly round, can fuse with each other, and exchange components with the cytoplasm. P granules are perinuclear during most of germline development and become cytoplasmic over the oocyte-to-embryo transition[12]. During the first embryonic cell cycle, P granules disassemble and re-assemble in the germ plasm, a region of cytoplasm in the posterior of the embryo that is partitioned to the germ lineage[11]. Several proteins have been implicated in P granule assembly. The RGG-domain protein PGL-3 and its paralog PGL-1 form a core condensate[13,14] that is recruited to the granules by the helicases LAF-1 and GLH-1 and the intrinsically disordered protein DEPS-1[13,15–17]. Assembly in germ plasm also requires two additional intrinsically disordered proteins: MEG-3 and its paralog MEG-4[18,19]. Lattice light-sheet microscopy of P granules in live wild-type embryos revealed that MEG-3 localizes to a structured phase enriched at the periphery of a more amorphous PGL-3-containing core, raising the possibility that P granules contain multiple phases with distinct material properties[19].

Here we have investigated the dynamic properties of PGL-1, PGL-3, LAF-1, GLH-1, DEPS-1, and MEG-3. We find that although several exhibit liquid-like properties, MEG-3 behaves uniquely like a gel-like polymer. We reconstituted a minimal P granule in vitro using MEG-3 and PGL-3, and find that MEG-3 forms gel-like condensates that associate with and stabilize liquid PGL-3 droplets.

Results

Proteins in P granules exhibit distinct dynamics. To examine P granule protein dynamics in live embryos, we used lines where the *meg-3, pgl-1, pgl-3, glh-1, deps-1*, or *laf-1* loci were tagged with green fluorescent protein (GFP) or mCherry using clustered regularly interspersed short palindromic repeats (CRISPR) genome editing (Supplementary Table 1). In the wild type, all six fusions enriched in condensates that localize to the posterior end of the one-cell embryo before the first division (Fig. 1a). In embryos where MEG-3 and its paralog MEG-4 were depleted by RNA-mediated interference (RNAi) or deleted by genome editing, all fusions became delocalized, and were distributed throughout the cytoplasm diffusely and in small condensates (PGL-1, PGL-3, GLH-1, and LAF-1) or in intense bright condensates (DEPS-1) (Fig. 1a and Supplementary Videos 1 and 2). These observations confirm that MEG-3 and MEG-4 are essential to assemble P granules in germ plasm.

To determine the rates of granule-to-cytoplasm exchange, we used fluorescence recovery after photobleaching (FRAP). As reported previously, PGL-1 and GLH-1 exhibited high rates of exchange (Fig. 1b and Supplementary Fig. 1a,b), consistent with co-localization in a liquid phase[11,20]. We found that PGL-3 and LAF-1 also exhibited high rates of exchange (Fig. 1b and Supplementary Fig. 1a,b). We could not detect any exchange for DEPS-1 (Supplementary Fig. 1b), but the relatively low levels of DEPS-1 on granules may have prevented detection of a low exchange rate. MEG-3 exhibited slow exchange dynamics (Fig. 1b and Supplementary Fig. 1a), an order of magnitude slower than PGL-1, PGL-3 and GLH-1, and two orders of magnitude slower than LAF-1 (Table 1). MBK-2 is a kinase that phosphorylates MEG-3 at the oocyte-to-embryo transition to promote dissolution of P granules in zygotes[19,21]. We found that MEG-3 dynamics decreased in embryos depleted of MBK-2 by RNAi (Fig. 1b and Supplementary Fig. 1h). In arrested oocytes, in which MBK-2 is not active, we detected no MEG-3 exchange over the timescale tested (Fig. 1b and Supplementary Fig. 1c). By contrast,

[1]Department of Molecular Biology and Genetics, Howard Hughes Medical Institute, Johns Hopkins University, School of Medicine, Baltimore, MD, USA. [2]Present address: Whitehead Institute, Massachusetts Institute of Technology, Boston, MA, USA. *e-mail: gseydoux@jhmi.edu
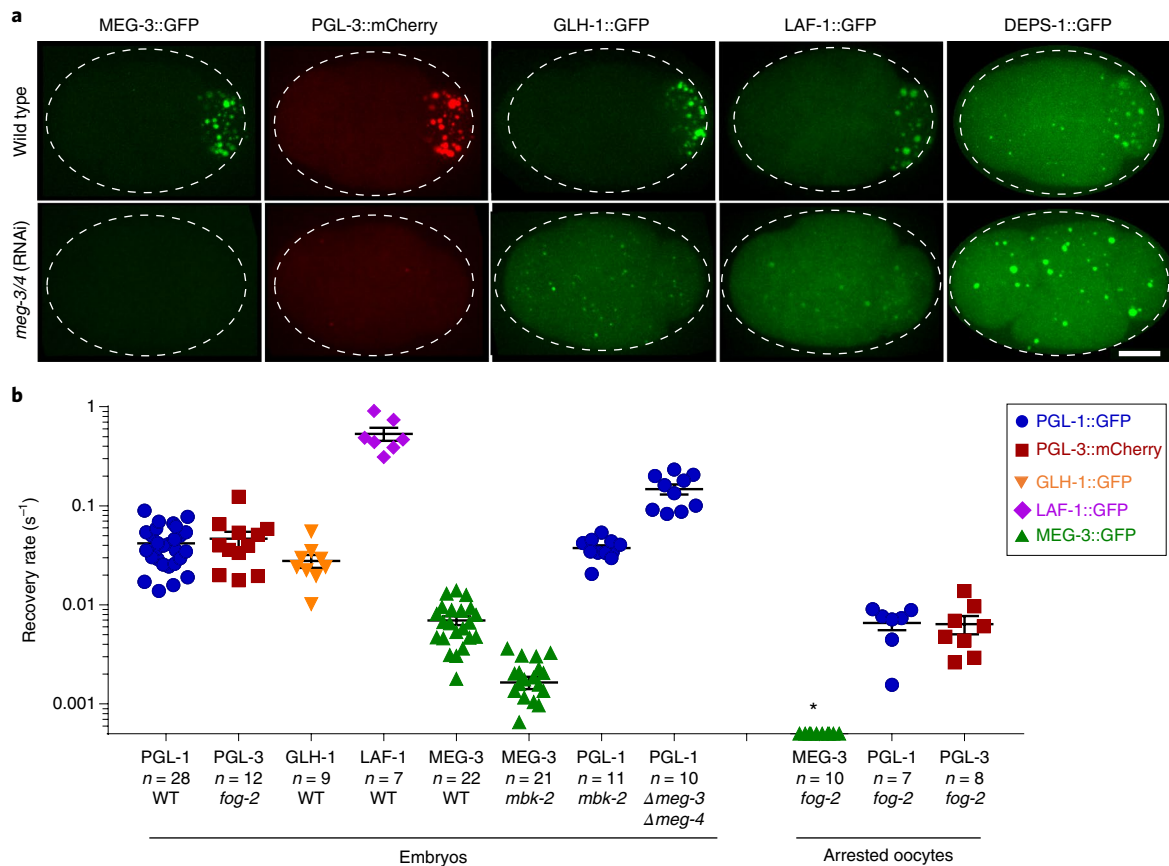
Fig. 1 | P granule proteins exhibit distinct dynamics. a, Photomicrographs of four-cell embryos co-expressing tagged MEG-3::GFP and PGL-3::mCherry or expressing single GFP-tagged P granule proteins (GLH-1::GFP, LAF-1::GFP, DEPS-1::GFP) in wild-type (WT) embryos or embryos depleted of MEG-3/4 by RNAi (see Supplementary Dataset 1 for *n* values). Scale bar, 10 μm. **b**, Recovery rates from the FRAP experiments plotted in Supplementary Fig. 1. Each symbol represents one FRAP experiment on one granule. The rate of fluorescence recovery (Methods) is plotted on the *y*-axis on a log scale. The *x*-axis indicates the P granule protein, genotype, and stage tested. *fog-2* is a feminizing mutation used here to arrest oocytes in the absence of sperm. Error bars represent mean ± s.e.m. calculated from independent experiments. *n* values are indicated in the *x*-axis label. For data points marked by an asterisk, no recovery was detected. Supplementary Fig. 1 shows recovery curves and photomicrographs of representative FRAP experiments. Source data are available in Supplementary Dataset 1.

**Table 1 | P granule protein dynamics in FRAP, temperature shift and extrusion assays**

P granule protein	FRAP recovery rate (s⁻¹)	$t_{1/2}$ (calculated from recovery rate, s⁻¹)	Temperature shift (20 °C→34 °C)	Extrusion assay
MEG-3::GFP	0.0070 ± 0.0007	128.3 ± 16.4	Stable	Stable
MEG-3::mCherry	0.0031 ± 0.0014	384.3 ± 198.8	Stable	Stable
PGL-1::GFP	0.042 ± 0.004	20.73 ± 2.0	Dissolves	Dissolves
PGL-3::mCherry	0.046 ± 0.008	21.9 ± 5.7	Dissolves	Dissolves
GLH-1::GFP	0.028 ± 0.004	30.1 ± 5.2	Dissolves	Dissolves
LAF-1::GFP	0.53 ± 0.08	1.5 ± 0.2	Stable	Dissolves
DEPS-1::GFP[a]	$<0.0001 s$	NA	Partially dissolves[a]	Partially dissolves[a]

This table summarizes results presented in Figs. 1–3 and Supplementary Figs. 1–3. FRAP values are reported as the mean ± s.e.m. See related figures for *n* values. NA, not calculated. [a]DEPS-1::GFP localizes to two types of condensates: a few small, bright condensates present throughout the cytoplasm, and many larger, dimmer and posteriorly localized condensates that correspond to P granules[16]. Both are reduced in intensity after temperature shift (Supplementary Fig. 3). After extrusion, only smaller, bright DEPS-1 condensates are visible (Supplementary Fig. 3).

PGL-1 and PGL-3 dynamics could still be detected in oocytes and were not affected by loss of MBK-2 (Fig. 1b and Supplementary Fig. 1c,e,g,i). PGL-1 dynamics, however, increased significantly in embryos lacking MEG-3 and MEG-4 (Fig. 1b and Supplementary Fig. 1j). We conclude that P granules contain at least two phases with distinct properties: a MEG-3 phase that becomes weakly dynamic in the transition from oocytes to embryos, and a constitutively dynamic, possibly liquid, PGL-containing phase that requires MEG-3 and MEG-4 for localization and stable assembly in embryos.

The MEG-3 phase is gel-like. Liquid phases are often more sensitive to changes in temperature and concentration than solid phases[22,23]. To test the effect of temperature, we filmed embryos co-expressing PGL-3::mCherry and MEG-3::GFP while subjecting them to rapid
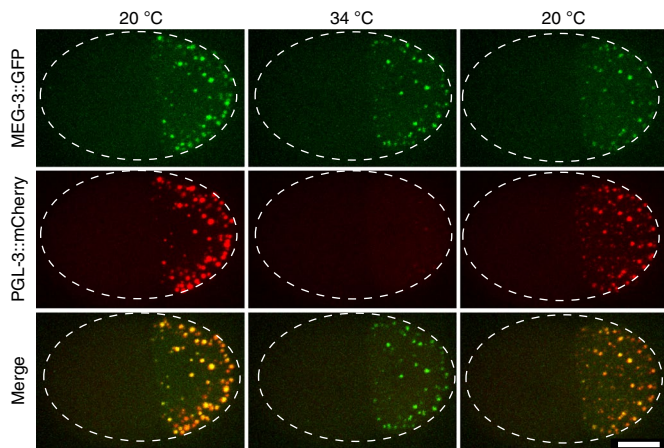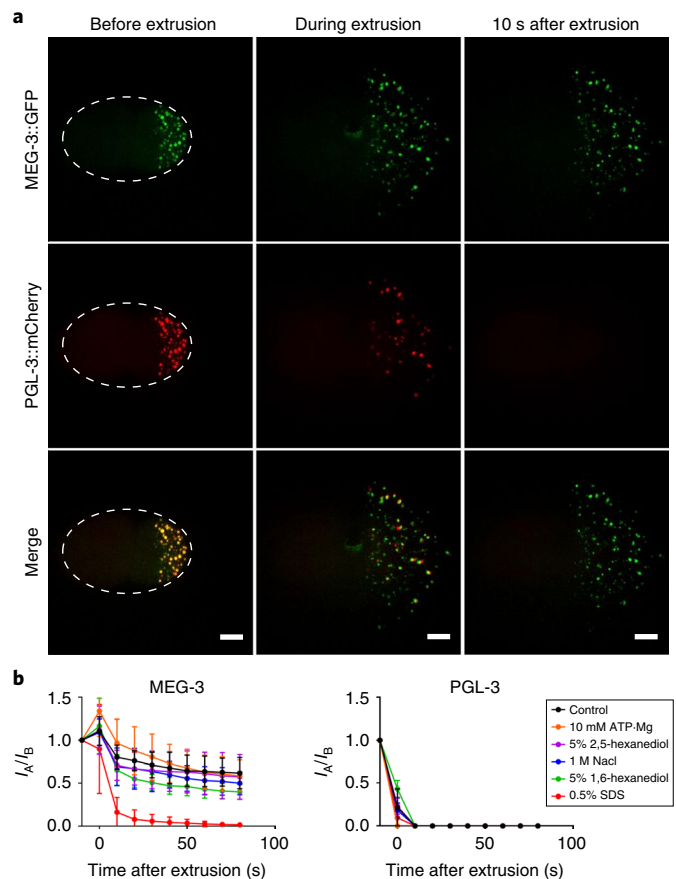
Fig. 2 | Effect of temperature on the MEG-3 and PGL-3 phases. Time-lapse photomicrographs of a two-cell embryo co-expressing MEG-3::GFP and PGL-3::mCherry fusions and cultured at 20 °C, upshifted to 34 °C for 1 min, and downshifted back to 20 °C for 8 min. Scale bar, 10 μm. Images are representative of six independent experiments.

Fig. 3 | Effect of dilution on the MEG-3 and PGL-3 phases. a, Time-lapse photomicrographs of a two-cell embryo co-expressing MEG-3::GFP and PGL-3::mCherry fusions before, immediately after (approximately 1 s), and 10 s after laser puncture of the eggshell. Laser puncture causes the contents of the posterior blastomere to spill onto the slide mixing with the aqueous buffer. Scale bar, 10 μm. **b**, Graphs showing the fraction of MEG-3::GFP or PGL-3::mCherry retained in the granular phase after extrusion. Total GFP or mCherry fluorescence from granules was measured before laser puncture (I_B) and after laser puncture (I_A) and used to calculate a fluorescence ratio (I_A/I_B). Means are indicated along with error bars representing s.d. calculated from multiple embryos (see Supplementary Dataset 1 for *n* values). Source data for **b** are available in Supplementary Dataset 1.

temperature shifts using a temperature-controlled stage. An upshift from 20 °C (normal growth temperature) to 34 °C caused PGL-3::mCherry to dissolve into the cytoplasm within seconds (Fig. 2). Returning the temperature to 20 °C caused PGL-3::mCherry to reappear on the granules after approximately 8 min (Fig. 2). By contrast, MEG-3::GFP remained in granules throughout the experiment. A longer 15 min shift to 34 °C also did not affect MEG-3::GFP distribution (Supplementary Fig. 2a). These distinct behaviors were not specific to the fluorescent tags as PGL-1::GFP also dissolved immediately when shifted to 34 °C, whereas MEG-3::mCherry remained in granules (Supplementary Fig. 2b). To test the effect of concentration, we punctured the eggshell of the embryo with a laser to release cellular contents into an aqueous buffer (Fig. 3a). Consistent with a liquid phase, PGL-3::mCherry diffused immediately on dilution into the buffer. By contrast, MEG-3::GFP persisted in the granule phase, as the granules flowed out of the embryo into the dilute buffer (Fig. 3b and Supplementaary Video 3). On average, 64 ± 18% of MEG-3::GFP fluorescence remained in the granule phase after extrusion (Fig. 3b). The extruded MEG-3::GFP granules persisted in the buffer for at least an hour (Supplementary Fig. 2c). MEG-3::GFP granules remained stable when extruded into buffer containing 1 M NaCl, 1,6-hexanediol (5%), or ATP, chemicals that dissolve liquid phases[24,25] (Fig. 3b). MEG-3::GFP granules, however, dissolved in SDS (0.5%) (Fig. 3b). PGL-3::mCherry dissolved in all buffers (Fig. 3b). These observations suggest that the MEG-3 phase is not an irreversible aggregate, but a stable, gel-like phase. By contrast, the PGL-3 phase behaves like a liquid.

The distinct behaviors of MEG-3 and PGL-3 were not specific to the tags (Supplementary Fig. 2d). PGL-1 and GLH-1 behaved like PGL-3 in the diffusion and extrusion assays (Supplementary Fig. 3a–c). LAF-1 and DEPS-1 each exhibited a unique set of behaviors (Supplementary Fig. 3a–c), but neither behaved as stably as MEG-3 in both assays (Table 1).

In vitro reconstitution of a minimal P granule. To determine whether the distinct properties of MEG-3 and PGL-3 observed in vivo are intrinsic to these proteins, we generated condensates in vitro using purified MEG-3 and PGL-3 (Supplementary Fig. 4a and Methods). Recombinant MEG-3 and PGL-3 were previously shown to phase separate with RNA under pH and salt conditions in the physiological range[18,26]. For all assays here, we used 0.15 μM MEG-3, 1.8 μM PGL-3, and 0.3 μM of total *C. elegans* RNA,

concentrations that respect the proportions of these components in embryos (Methods). To visualize each protein, we labeled a subset of MEG-3 and PGL-3 molecules with Dylight488 or Alexa647 respectively (Methods). As reported previously, when incubated separately in condensate buffer, MEG-3 and PGL-3 readily formed condensates (Fig. 4a). MEG-3 formed small condensates that ceased to grow almost immediately after a short assembly period (<1 min) (Fig. 4a–c and Supplementary Fig. 4b,c). The number and intensity of MEG-3 condensates remained stable over 30 min after assembly (Fig. 4b,c). Consistent with a non-dynamic phase, FRAP analyses revealed no exchange between MEG-3 condensates and the dilute phase, even when assayed within approximately 1 min of condensate formation, the earliest time we could access experimentally (Fig. 4d). By contrast, PGL-3 formed dynamic condensates with a recovery rate of $k_{rec}^{PGL-3} = 0.034 \pm 0.001\,s^{-1}$ (Fig. 4d and Supplementary Fig. 4d)[26] that increased in intensity and decreased in number over time, as expected for a liquid phase growing by Ostwald ripening and fusion (Fig. 4a–c and Supplementary Fig. 4b,c). When introduced together in condensate buffer, MEG-3 and PGL-3 initially formed separate condensates (1 min) (Fig. 4a and Supplementary Fig. 4e).
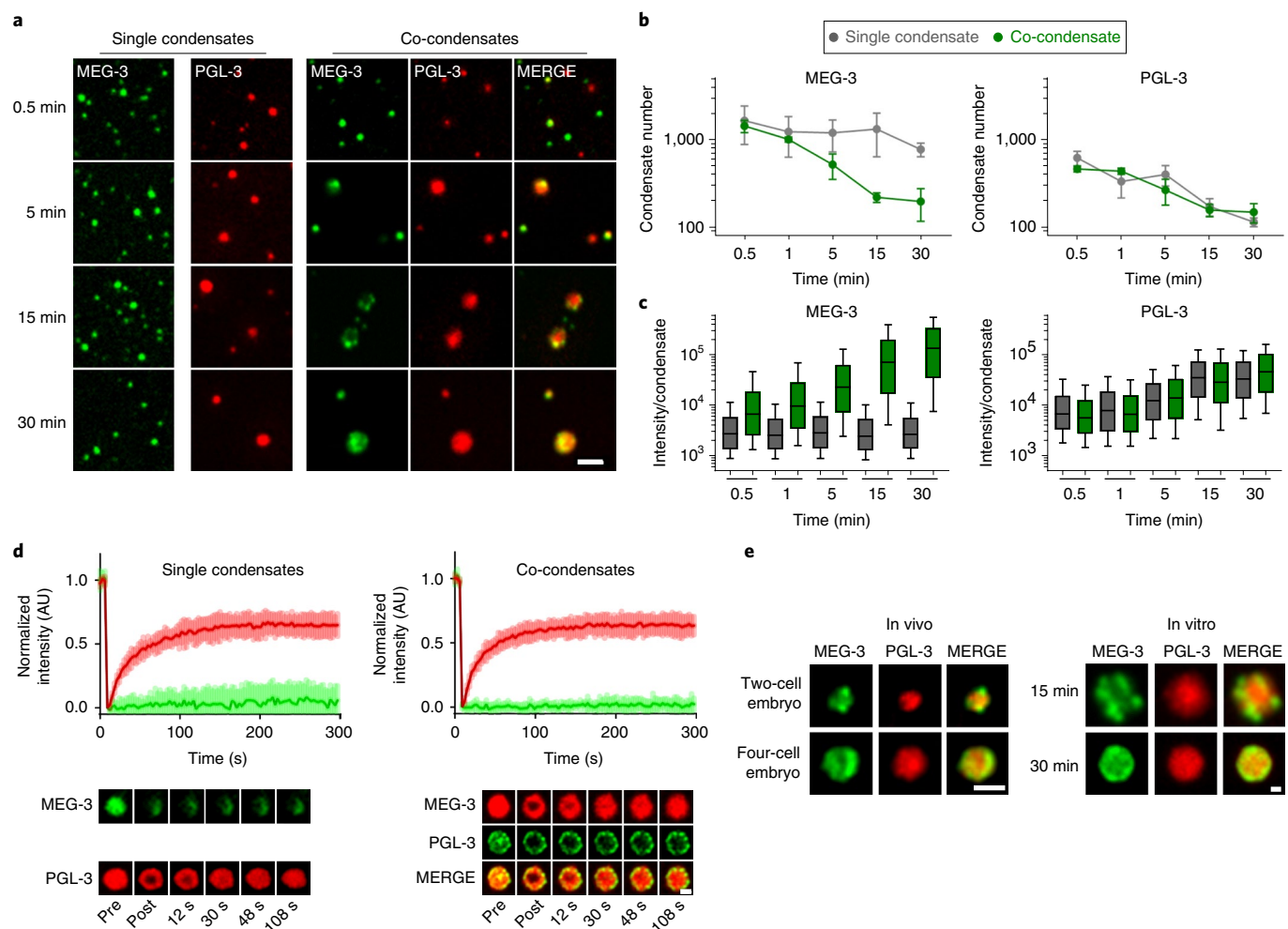
Fig. 4 | In vitro assembly of MEG-3 and PGL-3 condensates. a, Representative photomicrographs of MEG-3 and PGL-3 condensates after incubation in condensation buffer for the indicated times. MEG-3 was trace labeled with Dylight488 (green) and PGL-3 with Alexa647 (red) (Methods). Each image was adjusted separately to optimize visualization of small condensates in the first time point, and condensate substructure in the other time points. See Supplementary Fig. 4b for uniformly processed images. Images are representative of data quantified in **b** and **c**. Scale bars, 5 μm. **b**, Graphs showing the number condensates of MEG-3 or PGL-3 when incubated singly (gray) or together (green) at increasing time of incubation in condensate buffer. Each dataset includes condensates from 16 images collected from four experimental replicates. Circles indicate the mean and error bars represent the s.d. **c**, Graphs showing the distribution of total intensity of individual condensates of MEG-3 or PGL-3 when incubated singly (gray boxes) or together (green boxes) at increasing time of incubation in condensate buffer. Each dataset includes condensates from 16 images collected from four experimental replicates. Black lines indicate the mean, whiskers represent the entire range of the data, and bars represent the 90% confidence interval calculated from more than 500 condensates for each condition. **d**, FRAP of condensates assembled as in **a** and incubated for 30 min in condensate buffer. Granule intensity of MEG-3 or PGL-3 individual condensates (left, *n* = 8) or co-condensates (right, *n* = 7) was measured every 3 s for 300 s before and after bleaching. Values were normalized to initial fluorescence intensity, corrected for photobleaching and plotted as an average. Error bars represent mean ± s.d. Representative images are shown in the bottom panels. Scale bars, 1 μm. See Supplementary Fig. 4d for FRAP of fully bleached PGL-3 droplets. **e**, Representative photomicrographs of MEG-3 and PGL-3 co-condensates imaged in vivo in two- or four-cell embryos, or assembled in vitro. Scale bars, 1 μm. Representative in vivo images were selected from eight embryos. Representative in vitro condensates were selected from data quantified in **b** and **c**. Additional examples of MEG-3/PGL-3 condensates assembled in vivo are shown in Supplementary Fig. 5. Source data for **b**–**d** are available in Supplementary Dataset 1.

After 5 min of incubation, we begin to observe co-assemblies and by 30 min the majority of condensates contained both MEG-3 and PGL-3 (Fig. 4a and Supplementary Fig. 4e). During this period, the MEG-3 and PGL-3 condensates increased in intensity and decreased in number, as observed for PGL-3-only condensates (Fig. 4b,c). At early co-assembly time points, we could observe one or more distinct MEG-3 condensates on the surface of a PGL-3 droplet (Fig. 4a,e). After 30 min, more MEG-3 condensates accumulated around the PGL-3 phase (Fig. 4a,e and Supplementary Fig. 4f). In the co-condensates, the PGL-3 phase maintained rapid exchange with the surrounding dilute phase, as observed in PGL-3-only condensates (Fig. 4d). By contrast, we observed no exchange in the MEG-3

phase (Fig. 4d). The MEG-3 condensates, however, appeared to move relative to each other on the PGL-3 surface and the co-condensates could fuse (Supplementary Fig. 4g–i and Supplementary Videos 4–6). These observations suggest that the MEG-3 condensates do not interfere significantly with the liquid dynamics of the PGL phase.

To determine whether P granule assembly in vivo also involves interactions between MEG-3 and PGL-3 condensates, we imaged P granules in live embryos. In one- and two-cell embryos, we observed PGL-3 condensates surrounded by multiple, discrete smaller MEG-3 condensates (Fig. 4e and Supplementary Fig. 5a). By the four-cell stage, most PGL-3 droplets were surrounded by an uneven MEG-3
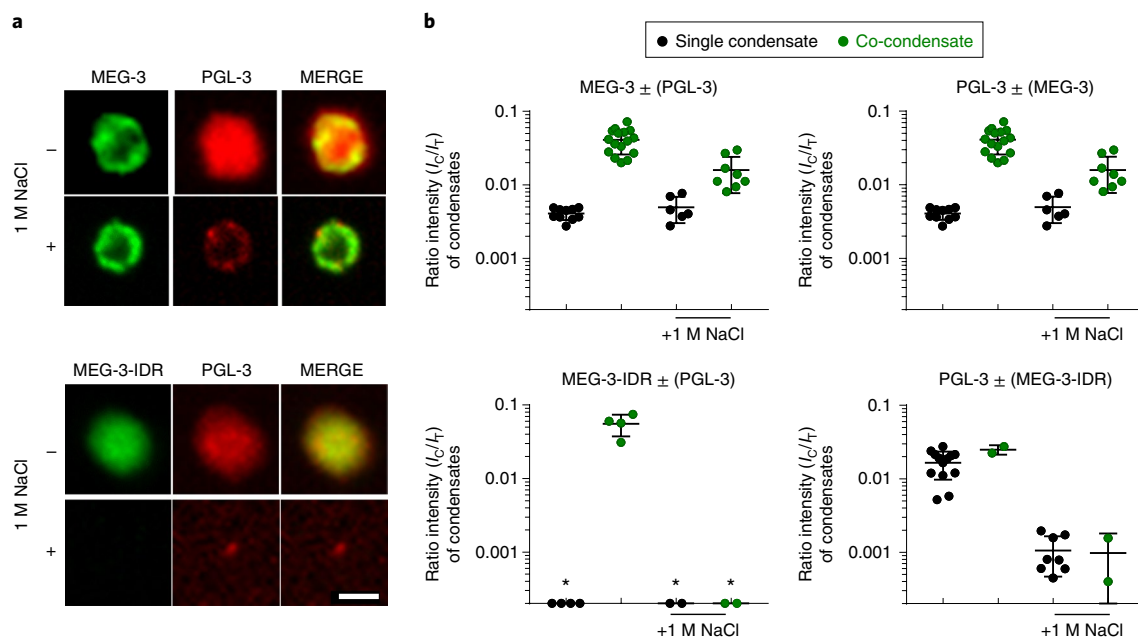
Fig. 5 | MEG-3 forms a stable scaffold around the PGL-3 liquid phase. a, Representative images of PGL-3 (red), MEG-3 (green) or MEG-3-IDR (green) co-assemblies incubated in condensation buffer or buffer with 1 M NaCl. Scale bars, 2 μm. Images are representative of data quantified in **b**. **b**, Graphs showing the relative proportion of PGL-3 (right), MEG-3 (top left), or MEG-3-IDR (bottom left) in condensates (calculated as the ratio of fluorescence in condensates (I_C) over total fluorescence (I_T)). The y-axis is on a log scale. Single condensates are in black and co-condensates are in green. Each data point represents the average from four images collected in one experiment. For data points indicated by asterisks, no condensates were detected. Bars represent the mean ± s.d. Source data for **b** are available in Supplementary Dataset 1.

layer (Fig. 5e and Supplementary Fig. 5b), as described previously[19]. Consistent with smaller MEG-3 condensates coalescing onto larger PGL-3 droplets, MEG-3 forms smaller granules in embryos lacking PGL-1 and PGL-3[18,19]. We conclude that co-assembly of PGL and MEG phases in vitro and in vivo involves accumulation of multiple MEG-3 condensates around growing PGL-3 droplets.
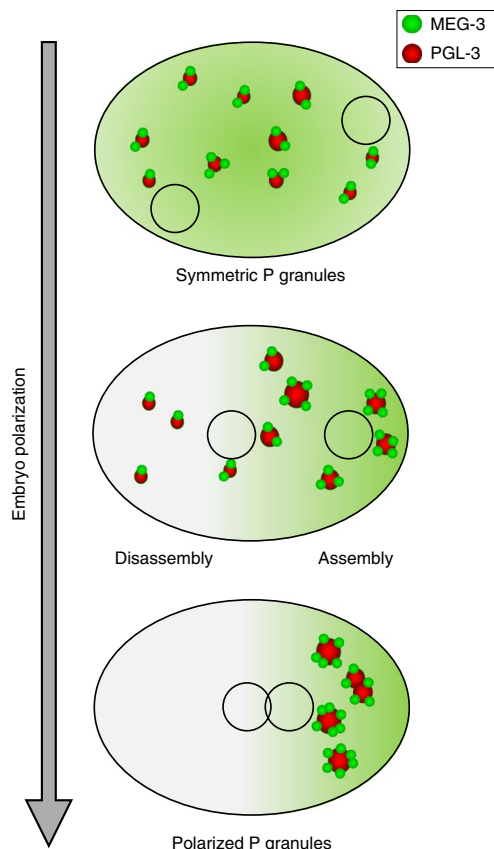
MEG-3 condensates stabilize PGL-3 condensates. As observed for MEG-3 ex vivo, MEG-3 condensates assembled in vitro were resistant to 1 M NaCl, 7 mM ATP, partially resistant to 5% 1,6-hexanediol, and sensitive to 0.5% SDS. PGL-3 condensates, by contrast, were sensitive to all these reagents (Fig. 5a,b and Supplementary Fig. 6a–d). In the co-condensates, MEG-3 showed the same range of resistance as in the single condensates and PGL-3 became partially resistant to 1 M salt, 7 mM ATP and 5% 1,6-hexanediol. The effect was most striking with 1 M NaCl. PGL-3 condensates dissolve almost completely in 1 M NaCl, but persisted partially in the co-condensates. After a 15 min incubation in 1 M NaCl, the co-condensates became 'hollow', losing most of the PGL-3-rich core, but retaining some PGL-3 foci in the MEG-3 ring (Fig. 5a,b and Supplementary Fig. 6b). We conclude that, as observed in vivo, the MEG-3 phase stabilizes the PGL-3 phase.

The intrinsically disordered N-terminal domain of MEG-3 is not sufficient to form gel-like condensates. MEG-3 contains a long (approximately 600 amino acids) predicted intrinsically disordered region (IDR) at its N terminus, and a shorter, predicted ordered domain at its C terminus. When expressed on its own from the *meg-3* locus, the MEG-3 IDR localizes to the germ plasm but is not sufficient to support granule formation under normal conditions[18]. We have shown previously that the IDR readily phase separates in vitro at concentrations greater than 1 μM[18]. We found, however, that at 0.15 μM, the MEG-3 IDR does not form visible condensates even in the presence of RNA (Fig. 5b and Supplementary Fig. 6a).

When mixed with RNA and PGL-3, the MEG-3 IDR was recruited into the PGL-3 condensates (Fig. 5b and Supplementary 6a), but did not form a distinct phase. Instead, the MEG-3 IDR distributed evenly throughout the PGL-3 condensate. MEG-3 IDR and PGL-3 co-condensates dissolved in 1 M NaCl, as do PGL-3-only condensates (Fig. 5). We conclude that formation of a stabilizing scaffold requires the MEG-3 C terminus in vitro, as it does in vivo.

Discussion

P granules were the first RNA granules proposed to be liquid droplets formed by LLPS[11]. The demonstration that certain P granule proteins undergo LLPS spontaneously in vitro lent support to this hypothesis[17,26], but the mechanisms that favor LLPS in the posterior of the embryo were not clear. A competition for RNA between PGL-3 and MEX-5, an RNA-binding protein enriched in the anterior[26], was proposed as a possible mechanism, but this model did not account for the role of MEG-3[18,27]. Our findings here suggest that the unique properties of the MEG-3 phase are what drive preferential LLPS of P granule proteins in the posterior cytoplasm (Fig. 6). MEG-3 forms stable, gel-like condensates that recruit PGL-3 molecules and associate with liquid PGL-3 droplets. In the co-condensates, the MEG-3 phase stabilizes the PGL-3 phase while maintaining the liquid dynamics necessary for granule growth. In embryos, posterior-enriched MEG-3 is required both for assembly of P granules in the posterior and disassembly of P granules in the anterior[18]. Our in vitro findings provide an explanation for this phenomenon: because the PGL phase remains in dynamic equilibrium with the cytoplasm in the co-condensates, stimulation of PGL condensation by posterior-enriched MEG-3 creates a posterior-directed flux of PGL molecules that destabilizes PGL droplets in the anterior cytoplasm. Artificial seeds that concentrate components of liquid phases are sufficient to promote LLPS in cells[28]. We suggest that the gel-like MEG-3 condensates function as biological seeds for P granules in the *C. elegans* germ plasm. Non-dynamic gel-like cores

Fig. 6 | Model for regulation of P granule assembly by the MEG-3 gel condensates. MEG-3 condensates associate dynamically with PGL-3 condensates. Polarization of the embryo enriches MEG-3 in the posterior cytoplasm[18]. Preferential stabilization of PGL-3 condensates in the posterior creates an anterior-to-posterior flux of PGL-3, which destabilizes PGL-3 condensates in the anterior.

have been reported in biomolecular condensates[9,10,29], but their significance has been debated. Our findings suggest that gel-like polymers are essential structural elements of biomolecular condensates that stimulate LLPS by increasing the local concentration of key components of liquid phases.

Online content

Any methods, additional references, Nature Research reporting summaries, source data, statements of data availability and associated accession codes are available at https://doi.org/10.1038/s41594-019-0193-2.

References

1. Hyman, A. A., Weber, C. A. & Julicher, F. Liquid–liquid phase separation in biology. *Annu. Rev. Cell Dev. Biol.* **30**, 39–58 (2014).
2. Boeynaems, S. et al. Protein phase separation: a new phase in cell biology. *Trends Cell Biol.* **28**, 420–435 (2018).
3. Shin, Y. & Brangwynne, C. P. Liquid phase condensation in cell physiology and disease. *Science* **357**, eaaf4382 (2017).
4. Han, T. W. et al. Cell-free formation of RNA granules: bound RNAs identify features and components of cellular assemblies. *Cell* **149**, 768–779 (2012).
5. Kato, M. et al. Cell-free formation of RNA granules: low complexity sequence domains form dynamic fibers within hydrogels. *Cell* **149**, 753–767 (2012).
6. Lin, Y., Protter, D. S., Rosen, M. K. & Parker, R. Formation and maturation of phase-separated liquid droplets by RNA-binding proteins. *Mol. Cell* **60**, 208–219 (2015).
7. Molliex, A. et al. Phase separation by low complexity domains promotes stress granule assembly and drives pathological fibrillization. *Cell* **163**, 123–133 (2015).
8. Taylor, J. P., Brown, R. H. Jr & Cleveland, D. W. Decoding ALS: from genes to mechanism. *Nature* **539**, 197–206 (2016).
9. Jain, S. et al. ATPase-modulated stress granules contain a diverse proteome and substructure. *Cell* **164**, 487–498 (2016).
10. Wheeler, J. R., Matheny, T., Jain, S., Abrisch, R. & Parker, R. Distinct stages in stress granule assembly and disassembly. *eLife* **5**, e18413 (2016).
11. Brangwynne, C. P. et al. Germline P granules are liquid droplets that localize by controlled dissolution/condensation. *Science* **324**, 1729–1732 (2009).
12. Strome, S. in *WormBook* (ed. The *C. elegans* Research Community) https://doi.org/10.1895/wormbook.1.9.1 (2005).
13. Hanazawa, M., Yonetani, M. & Sugimoto, A. PGL proteins self associate and bind RNPs to mediate germ granule assembly in *C. elegans*. *J. Cell Biol.* **192**, 929–937 (2011).
14. Kawasaki, I. et al. The PGL family proteins associate with germ granules and function redundantly in *Caenorhabditis elegans* germline development. *Genetics* **167**, 645–661 (2004).
15. Spike, C. et al. Genetic analysis of the *Caenorhabditis elegans* GLH family of P-granule proteins. *Genetics* **178**, 1973–1987 (2008).
16. Spike, C. A., Bader, J., Reinke, V. & Strome, S. DEPS-1 promotes P-granule assembly and RNA interference in *C. elegans* germ cells. *Development* **135**, 983–993 (2008).
17. Elbaum-Garfinkle, S. et al. The disordered P granule protein LAF-1 drives phase separation into droplets with tunable viscosity and dynamics. *Proc. Natl Acad. Sci. USA* **112**, 7189–7194 (2015).
18. Smith, J. et al. Spatial patterning of P granules by RNA-induced phase separation of the intrinsically disordered protein MEG-3. *eLife* **5**, e21337 (2016).
19. Wang, J. T. et al. Regulation of RNA granule dynamics by phosphorylation of serine-rich, intrinsically disordered proteins in *C. elegans*. *eLife* **3**, e04591 (2014).
20. Sheth, U., Pitt, J., Dennis, S. & Priess, J. R. Perinuclear P granules are the principal sites of mRNA export in adult *C. elegans* germ cells. *Development* **137**, 1305–1314 (2010).
21. Pellettieri, J., Reinke, V., Kim, S. K. & Seydoux, G. Coordinate activation of maternal protein degradation during the egg-to-embryo transition in *C. elegans*. *Dev. Cell* **5**, 451–462 (2003).
22. Weber, S. C. & Brangwynne, C. P. Getting RNA and protein in phase. *Cell* **149**, 1188–1191 (2012).
23. Banani, S. F., Lee, H. O., Hyman, A. A. & Rosen, M. K. Biomolecular condensates: organizers of cellular biochemistry. *Nat. Rev. Mol. Cell Biol.* **18**, 285–298 (2017).
24. Patel, A. et al. ATP as a biological hydrotrope. *Science* **356**, 753–756 (2017).
25. Lin, Y. et al. Toxic PR poly-dipeptides encoded by the C9orf72 repeat expansion target LC domain polymers. *Cell* **167**, 789–802.e712 (2016).
26. Saha, S. et al. Polar positioning of phase-separated liquid compartments in cells regulated by an mRNA competition mechanism. *Cell* **166**, 1572–1584. e1516 (2016).
27. Seydoux, G. The P granules of *C. elegans*: a genetic model for the study of RNA–protein condensates. *J. Mol. Biol.* **430**, 4702–4710 (2018).
28. Bracha, D. et al. Mapping local and global liquid phase behavior in living cells using photo-oligomerizable seeds. *Cell* **175**, 1467–1480.e1413 (2018).
29. Woodruff, J. B., Hyman, A. A. & Boke, E. Organization and function of non-dynamic biomolecular condensates. *Trends Biochem. Sci.* **43**, 81–94 (2018).

Acknowledgements

Author contributions

A.P., M.C., J.S., and G.S. designed the research. A.P. and M.C. performed all experiments, collected, and analyzed data. G.S. and A.P. prepared the manuscript with contributions from all authors.

Competing interests

The authors declare no competing interests.

Methods

Strain maintenance and RNAi. *C. elegans* was cultured according to standard methods at 20 °C unless otherwise stated[30]. Genome editing was performed using CRISPR–Cas9 as previously described[31]. Strains used in this study are listed in Supplementary Table 1.

mbk-2 or *meg-3meg-4* (RNAi) was performed by feeding[32] using plasmids from the Ahringer or Open Biosystems libraries . HT115 bacteria transformed with feeding vectors were grown at 37 °C in LB medium with ampicillin (100 µg ml⁻¹) for 5 h, induced with 5 mM IPTG for 45 min, plated on NNGM (nematode nutritional growth media) with ampicillin (100 µg ml⁻¹) and IPTG (1 mM), and grown overnight at room temperature. For *mbk-2* RNAi, embryos were hatched on RNAi plates and allowed to feed for approximately 3–4 days. For *meg-3meg-4* RNAi, L4 larvae were fed at 20 °C for 24–40 h.

For visualization of arrested oocytes, *fog-2 (q71)* females (which do not produce sperm) were collected in the L4 stage and matured for 8 h before imaging in 20 nM levamisole. For imaging of embryos, adult hermaphrodites were dissected in 1× ex vivo buffer (25 mM HEPES, pH 7, 150 mM NaCl, 2 mM CaCl₂, 2 mM MgCl₂) to release embryos which were mounted onto 2% agarose pads on glass slides.

Microscopy. Images shown in Figs. 1–3, 4a,e and 5 and Supplementary Figs. 1–3, 5b,g,h, 6 and 7 were captured with a Zeiss Axio Imager equipped with a Yokogawa spinning-disc confocal scanner and Slidebook v.6.0 software (Intelligent Imaging Innovations). Unless otherwise noted, embryo and oocyte images are *Z*-stack maximum projections using a *Z*-step size of 1 µm, spanning the depth of the oocyte or embryos using a 60× objective. In vitro granule images or videos are single planes taken using a 60× objective (Figs. 4a,e and 5a,b and Supplementary Figs. 4b,6a,b and 40× objective (Supplementary Fig. 4g,h and Supplementary Videos 4 and 5). Images shown in Fig. 4e (right) and Supplementary Fig. 5 were captured with a GE OMX-SR microscope with Aquire SR software and deconvoluted with softWoRx software. Embryo images are *Z*-stack maximum projections using a *Z*-step size of 0.125 µm, spanning the depth of the embryo. Images of enlarged granules are single planes. Images were acquired using 90 ms exposures in the 488 channel and 65 ms exposures in the 561 channel using a 60× objective. Images shown in Fig. 4d, Supplementary Fig. 4,i and Supplementary Video 6 were captured with using a Zeiss LSM 800 GaAsp system. Images are single confocal planes imaged using a 63× objective every 1–3 s during a recovery phase of 300 s with a laser power of 0.3–0.5% and a gain of 600–700. All image analyses were conducted using the Fiji image-processing package (http://fiji.sc/Fiji).

FRAP. In vivo: photobleaching of P granule proteins in oocytes or embryos was performed using a laser to bleach a region slightly larger than the area of the granule (2 µm diameter) in the center plane of the *Z*-stack. Images were acquired as *Z*-stacks with ten planes with a step size 1 µm (oocytes) or 11 planes with a step size of 0.6 µm (embryos) by imaging 50 ms exposures for all proteins in oocytes and MEG-3::GFP, LAF-1::GFP, DEPS-1::GFP in embryos, 25 ms exposures for PGL-3::mCherry, PGL-1::GFP, GLH-1::GFP in embryos, and 300 ms exposures for MEG-3::mCherry in embryos using a 63× objective. In oocytes, images were acquired every 5 s. In embryos, images were acquired every 3 s (PGL-1::GFP, GLH-1::GFP, LAF-1::GFP), 5 s (MEG-3::GFP, DEPS-1::GFP, PGL-3::mCherry), or 7 s (MEG-3::mCherry) during a recovery phase of 180–300 s after photobleaching.

In vitro: 20 µl condensation reaction (prepared as described below (in the Methods subsection 'In vitro condensation experiments') were added to a chambered coverglass (Grace BioLabs) and imaged using a Zeiss LSM 800 GaAsp system. Bleaching was performed using 100% laser power in the 488 and 647 channels for MEG-3-Dylight 488 or PGL-3-Alexa 647, respectively. Regions of slightly larger than the condensates (radius ≈ 2.5 µM) or regions within condensates (radius ≈ 1 µM) were photobleached. A single confocal plane was imaged using a 63× objective every 3 s during a recovery phase of 300 s with a laser power of 0.3–0.5% and a gain of 600–700.

Maximum projections of *Z*-stacks acquired as above were analyzed in Fiji. The total or mean fluorescence intensity of the area containing the granule was measured at each time point. Fluorescence recovery was corrected for background and normalized to the initial granule intensity using the equation: $I^n = (I - I^{bkg}) / (I^i - I^{bkgi})$, where I^n is the background corrected and normalized fluorescence intensity, I is the intensity of the granule subjected to FRAP, I^{bkg} is the fluorescence intensity of the cytoplasm that is not subjected to FRAP, I^i is the initial intensity of the granule subjected to FRAP before bleaching, and I^{bkgi} is the initial background intensity. For in vitro FRAP, the normalized intensity was corrected for photobleaching using the average photobleaching rate calculated from condensates not subjected to FRAP in the imaging area. Photobleaching was minimal in embryos and oocytes over the time course of the experiment (<10%) except for LAF-1::GFP. For the LAF-1 experiments, the normalized intensity was corrected for photobleaching using the average photobleaching rate from a region not subjected to FRAP of the cytoplasm in the imaging area. Recovery rates were determined by fitting individual traces to a first-order equation $I^n = (A^{rec}(1 - e^{-kt}))$. Where A^{rec} is the fluorescence recovery amplitude and k is the rate of fluorescence recovery. For MEG-3::GFP FRAP experiments in *mbk-2* (RNAi) embryos where amplitudes only just approached full recovery during the time frame of the experiment, final recovery amplitudes were limited to $A^{rec} = 1$.

Temperature shifts. Temperature-shift experiments were performed on a fluidic temperature-control stage that enabled rapid temperature shifts (CherryTemp, CherryBiotech). Embryos were prepared as described for FRAP experiments. Images were acquired using a *Z*-step size of 1 µm, spanning the entire depth of the embryo. Final images are *Z*-stack maximum projections. Images were taken every 15 s broken into the following segments: 1 min at 20 °C followed by a 3–15 min shift to 34 °C and then returned to 20 °C for 25 min.

Ex vivo experiments. All ex vivo buffers were prepared in 25 mM HEPES pH 7, 150 mM NaCl, 2 mM CaCl₂, 2 mM MgCl₂ buffered to pH 7.0 with NaOH and HCl using a Mettler Toledo Seveneasy pH meter and a Fisherbrand Accumet glass-body, standard-combination, mercury-free electrode. Embryos were dissected from adult hermaphrodites in ex vivo buffer and mounted on glass slides with 3% agarose pads made with 1× ex vivo buffer. Embryo contents were extruded by puncturing the eggshell near the anterior region of the germline blastomere using a 3i Ablate! laser system at 532 nm pulse setting with a power level of 155. All embryo images are *Z*-stack maximum projections using a *Z*-step size of 1 µm, spanning the entire depth of the embryo. Images were acquired using 50 ms exposures in the 488 channel and/or 50 ms exposures in the 561 channel every 10 s using a 63× objective. For MEG-3::mCherry, the 561 laser power was reduced to 50% and 300 ms exposures were taken owing to low fluorescence signal. For Supplementary Fig. 2 c, images were taken every 15 min for 60 min following extrusion.

To quantify MEG-3::GFP persistence in granules, photomicrographs acquired as described above were analyzed using ImageJ64. Background was subtracted from each image using a rolling ball radius of 50 pixels. Pixels were smoothed one time and images were converted to 8-bit. The pixel brightness threshold was set to 50–255 and the total integrated density of the objects (MEG-3::GFP granules) was quantified. Total fluorescence intensity was calculated before (I_B) and after (I_A) extrusion and used to calculate a fluorescence ratio (I_A/I_B). For some embryos, granules left the field of view and could not be counted. The I_A/I_B, therefore, is a minimal estimate of the fraction of MEG-3::GFP that remains in the granule phase after extrusion.

Protein purification and labeling. Overview: MEG-3 was purified from *Escherichia coli* under denaturing conditions as a His-tagged fusion or under native conditions as an MBP fusion followed by protease removal of MBP (Supplementary Fig. 4a). No significant differences were noted between the two purification methods. PGL-3 was purified from *E. coli* as an MBP fusion followed by protease removal of MBP (Supplementary Fig. 4a).

Purification of MEG-3 His-tagged fusion: MEG-3 full-length (amino acids 1–862) and MEG-3_IDR (amino acids 1–698) fused to an N-terminal 6×His tag in pET28a were expressed and purified from inclusion bodies using a denaturing protocol as described[18].

Purification of MBP fusions: MBP-TEV-PGL-3 or MBP-TEV-MEG-3 were expressed in Rosetta (DE3) cells at 16 °C in terrific broth with ampicillin (100 µg ml⁻¹) to an OD₆₀₀ₙₘ of approximately 1.0 and induced with 1 mM IPTG at 16 °C for 16 h. Cells were resuspended in buffer A (25 mM HEPES pH 7.4, 500 mM NaCl, 0.4 M L-arginine, 20% (v/v) glycerol, 1 mM DTT) with added protease inhibitors, 5 µg ml⁻¹ RNase A (USB), 0.25 U µl⁻¹ RNase I (Ambion), lysed by sonication, spun at 29,000*g* for 15 min. Lysates were filtered and passed over a MBPTrap column (GE Healthcare). The resin was washed with buffer B1000 (25 mM HEPES pH 7.4, 40% (v/v) glycerol, 1 mM DTT, 1,000 mM NaCl). Protein was eluted in Buffer B1000 and 20 mM Maltose. Solutions were diluted twofold with buffer B with 0 mM NaCl (B0) for a final concentration of 500 mM NaCl. Four-hundred units of ProTEV protease (Promega) was added per mg of protein for 2–4 h at room temperature to remove the MBP tag. Solutions were diluted to 200 mM NaCl with buffer B0, and immediately loaded onto a HeparinTrap column (GE Healthcare). Proteins were washed and eluted with a stepwise gradient made by mixing buffer B0 with B1000. Untagged PGL-3 and MEG-3 were eluted in 500 and 800 mM NaCl, respectively. Protein-containing fractions were flash frozen in small aliquots in liquid nitrogen, and stored at −80 °C.

Protein labeling: proteins were labeled with succinimidyl-ester-reactive fluorophores from Molecular Probes (Alexa Fluor 647 NHS or DyLight 488 NHS Ester) according to the manufacturer's instructions. Free fluorophore was eliminated by passage through three Zeba Spin Desalting Columns (7K MWCO, 0.5 ml) into protein storage buffer. The concentration of fluorophore-labeled protein was determined using fluorophore extinction coefficients. Labeling reactions resulted in approximately 0.25–1 label per protein. Aliquots were snap frozen and stored. In phase-separation experiments, fluorophore-labeled protein was mixed with unlabeled protein for final reaction concentrations of 25–100 nM of fluorophore.

RNA preparation. Total RNA was extracted from a *C. elegans* culture using TRIzol (Invitrogen) following published methods. Poly-A selected RNA was prepared using Dynabeads Oligo(dT)₂₅ (ThermoFisher) using two rounds of selection.

In vitro condensation experiments. Protein condensation was induced by diluting proteins out of storage buffer into condensation buffer containing 25 mM HEPES (pH 7.4), NaCl adjusted to a final concentration of 150 mM, and RNA.

For experiments shown in Figs. 4 and 5 and Supplementary Figs. 4 and 6 total competing endogenous RNA was denatured at 95 °C for 30 s and added to the condensation buffer to a final concentration of 150 ng μl^{-1}. For data included in Fig. 5b and Supplementary Fig. 6c,d replicates included poly-A-selected RNA used at a concentration of 150 ng μl^{-1}.

The concentrations of MEG-3, PGL-3 and mRNA have been estimated at 11 ± 4 nM, 680 ± 200 nM and 100 nM (50 ng μl^{-1}), respectively[26]. These estimates were derived from pooled, mixed-stage embryos and thus are likely to be underestimates for MEG-3 and PGL-3, since these proteins are concentrated in just one cell per embryo, and are not present after the 100-cell stage in the case of MEG-3. We tested a range of concentrations in co-assembly experiments and found that MEG-3/PGL-3 condensates form over a wide range of concentrations as long as the ratio of RNA to MEG-3 is kept high to prevent co-assemblies of PGL-3 and MEG-3 from aggregating (Supplementary Fig. 7). Unless otherwise indicated, for all co-assembly experiments, we used 150 nM MEG-3/MEG-3-Dylight488, 1.8 μM PGL-3/PGL-3-Alexa647 and 300 nM (150 ng μl^{-1}) RNA. Altering the order of addition did not affect co-condensate assembly. Condensation reactions were incubated at room temperature for 30 min or less as indicated, before spotting onto thin-chambered glass slides (Erie Scientific 30-2066A) with a coverslip. Condensates were imaged using a Zeiss Axio Imager equipped with a Yokogawa spinning-disc confocal scanner and Slidebook v.6.0 software (Intelligent Imaging Innovations). Images used for quantification are single planes acquired using a 40× oil objective over an area spanning 171 × 171 μm^2. For Supplementary Videos 4–6 slides were treated with PEG-silane[33].

To quantify the ratio of MEG-3-Dylight or PGL-3-Alexa647 in condensates, a mask was created by thresholding images, filtering out objects of less than 2 pixels to minimize noise, and applying a watershed filter to improve separation of condensates close in proximity, and converted to a binary image by the Otsu method using the nucleus counter cookbook plugin in Fiji. Minimum thresholds were set to the mean intensity of the background signal of the image. The maximum threshold was calculated by adding two times the s.d. of the background. To develop a mask to measure co-condensate assembly, individual channels of MEG-3-Dylight488 and PGL-3-Alexa647 images were set to thresholds as described above and averaged. The resulting image was processed as described above to generate the co-condensate mask. Using generated masks, the integrated intensity within each condensate was calculated. To remove non-specific background signal the mean intensity of an image field in the absence of the labeled protein was subtracted from each pixel yielding the total intensity of each condensate. To calculate the ratio in condensates, the sum of intensities of all condensates in an imaged area (I_c) was divided by the total intensity of the imaged area (I_T). Each data point represents data from four images acquired in a single experiment.

To quantify co-localization of MEG-3 and PGL-3 in co-condensates over time, the covariance of MEG-3 and PGL-3 intensity within condensates measured using the co-condensate mask were compared using the Pearson's correlation coefficient. Data points represent the mean ± s.d. of coefficients calculated for a total of 16 images from four experimental replicates.

Radial profile plot. To quantify the heterogeneity of the MEG-3 and PGL-3 phases of the condensates, a radial profile plot was generated using the oval profile plugin in ImageJ64. A region centered on and slightly larger than the condensate was drawn. The maximum intensity of radii extending from the center of the region to the exterior in 3° increments was calculated, the mean background was subtracted and intensities were normalized to the maximum intensity and plotted for PGL-3 and MEG-3. The resulting plot shows the variation in intensity around the circumference of the condensate.

Graphing and data fitting. All data were plotted and statistical analysis was conducted using Graphpad Prism 7 software. Fitting of recovery curves in FRAP experiments was conducted using Kaleidagraph (Synergy) software.

Reporting Summary. Further information on research design is available in the Nature Research Reporting Summary linked to this article.

Data availability
Source data for Figs. 1 and 3–5 and Supplementary Fig. 3 are available in Supplementary Dataset 1. Other data supporting the findings of this study are available from the corresponding author upon reasonable request.

References
30. Brenner, S. The genetics of *Caenorhabditis elegans*. *Genetics* **77**, 71–94 (1974).
31. Paix, A., Folkmann, A., Rasoloson, D. & Seydoux, G. High efficiency, homology-directed genome editing in *Caenorhabditis elegans* using CRISPR–Cas9 ribonucleoprotein complexes. *Genetics* **201**, 47–54 (2015).
32. Timmons, L. & Fire, A. Specific interference by ingested dsRNA. *Nature* **395**, 854 (1998).
33. Alberti, S. et al. A user's guide for phase separation assays with purified proteins. *J. Mol. Biol.* **430**, 4806–4820 (2018).

Corresponding author(s):   Geraldine Seydoux, Andrea Putnam

Reporting Summary

Nature Research wishes to improve the reproducibility of the work that we publish. This form provides structure for consistency and transparency in reporting. For further information on Nature Research policies, see Authors & Referees and the Editorial Policy Checklist.

Statistical parameters

When statistical analyses are reported, confirm that the following items are present in the relevant location (e.g. figure legend, table legend, main text, or Methods section).

n/a	Confirmed	
☐	☒	The exact sample size (n) for each experimental group/condition, given as a discrete number and unit of measurement
☐	☒	An indication of whether measurements were taken from distinct samples or whether the same sample was measured repeatedly
☐	☒	The statistical test(s) used AND whether they are one- or two-sided *Only common tests should be described solely by name; describe more complex techniques in the Methods section.*
☐	☒	A description of all covariates tested
☐	☒	A description of any assumptions or corrections, such as tests of normality and adjustment for multiple comparisons
☐	☒	A full description of the statistics including central tendency (e.g. means) or other basic estimates (e.g. regression coefficient) AND variation (e.g. standard deviation) or associated estimates of uncertainty (e.g. confidence intervals)
☐	☒	For null hypothesis testing, the test statistic (e.g. F, t, r) with confidence intervals, effect sizes, degrees of freedom and P value noted *Give P values as exact values whenever suitable.*
☒	☐	For Bayesian analysis, information on the choice of priors and Markov chain Monte Carlo settings
☒	☐	For hierarchical and complex designs, identification of the appropriate level for tests and full reporting of outcomes
☐	☒	Estimates of effect sizes (e.g. Cohen's d, Pearson's r), indicating how they were calculated
☐	☒	Clearly defined error bars *State explicitly what error bars represent (e.g. SD, SE, CI)*

Our web collection on statistics for biologists may be useful.

Software and code

Policy information about availability of computer code

Data collection	GE OMX-SR microscope with Aquire SR software and deconvoluted with softWoRx software, Zeiss LSM 800 GaAsp data acquired with Zen (Blue edition) software, Zeiss Axio Imager equipped with a Yokogawa spinning-disc confocal scanner and Slidebook v 6.0 software (Intelligent Imaging Innovations)
Data analysis	ImageJ64 (1.50b), Fiji (ImageJ1.51w),Graphpad Prism 7, Kaleidagraph 3.52 (Synergy)

For manuscripts utilizing custom algorithms or software that are central to the research but not yet described in published literature, software must be made available to editors/reviewers upon request. We strongly encourage code deposition in a community repository (e.g. GitHub). See the Nature Research guidelines for submitting code & software for further information.

Data

Policy information about availability of data

All manuscripts must include a data availability statement. This statement should provide the following information, where applicable:

- Accession codes, unique identifiers, or web links for publicly available datasets
- A list of figures that have associated raw data
- A description of any restrictions on data availability

The datasets generated during and/or analysed during the current study are available from the corresponding author on reasonable request.

Field-specific reporting

Please select the best fit for your research. If you are not sure, read the appropriate sections before making your selection.

☒ Life sciences ☐ Behavioural & social sciences ☐ Ecological, evolutionary & environmental sciences

For a reference copy of the document with all sections, see nature.com/authors/policies/ReportingSummary-flat.pdf

Life sciences study design

All studies must disclose on these points even when the disclosure is negative.

Sample size	No sample-size calculations were performed. Sample size was determined to be adequate based on the magnitude and consistency of measurable differences between groups.
Data exclusions	On principle, data were only excluded for failed experiments, reasons for which included poor image quality, temperature variation, ineffective RNAi treatment.
Replication	Replicate experiments were successful.
Randomization	Samples were not randomized. C. elegans were analyzed at comparable life stages and treatments. For RNAi experiments, control and treated strains came from the same stock.
Blinding	Investigators were not blinded to genotypes during experiments. Data reported for experiments are not subjective but based on quantitative analysis.

Reporting for specific materials, systems and methods

Materials & experimental systems

n/a	Involved in the study
☒	☐ Unique biological materials
☒	☐ Antibodies
☒	☐ Eukaryotic cell lines
☒	☐ Palaeontology
☐	☒ Animals and other organisms
☒	☐ Human research participants

Methods

n/a	Involved in the study
☒	☐ ChIP-seq
☒	☐ Flow cytometry
☒	☐ MRI-based neuroimaging

Animals and other organisms

Policy information about studies involving animals; ARRIVE guidelines recommended for reporting animal research

Laboratory animals	Supplementary Table 1 provided with manuscript contains information on all C. elegans strains used in this study.
Wild animals	The study did not involve wild animals.
Field-collected samples	The study did not involve samples collected from the field.